Experimental and numerical study of a two-body heaving wave energy converter with different power take-off models

Xiaochen Dong[a], Zhen Gao[b], Demin Li[a], Hongda Shi[a,c,d,*]

[a] *Department of Ocean Engineering, College of Engineering, Ocean University of China, Qingdao 266100, China*

[b] *Department of Marine Technology and Centre for Autonomous Marine Operations and Systems (AMOS), Norwegian University of Science and Technology (NTNU), Trondheim, 7491, Norway*

[c] *Shandong Provincial Key Laboratory of Ocean Engineering, Ocean University of China, Qingdao 266100, China*

[d] *Qingdao Municipal Key Laboratory of Ocean Renewable Energy, Ocean University of China, Qingdao 266100, China*

Abstract

Wave energy is one of the most difficult energies to be captured among marine renewables. With the technical progress, wave energy converters (WECs) are being tested in relatively deeper waters, which makes floating concepts almost the only choice. In this paper, a two-body heaving WEC where the wave energy is absorbed through the relative motion between the outer annular and the inner cylindrical buoys is studied. Both experimental and numerical studies are adopted for regular wave conditions. In the physical model test, a hydraulic system is used to achieve constant power take-off (PTO) damping force. Numerical simulations, validated against experimental data, are applied using both the frequency domain and the time domains analyses. Different types of PTOs,

[*] Corresponding author: Hongda Shi, College of Engineering, Ocean University of China, 238, Songling Road, 266100, China. E-mail address: hongda.shi@ouc.edu.cn

including constant, linear and nonlinear damping forces, are undertaken to evaluate the hydrodynamic and power absorption performance of such device.

Keywords: two-body heaving wave energy converter; physical model test; numerical simulation; power take-off.

1 Introduction

According to the *Vision for International Deployment of Ocean Energy* by OES (2018), the global potential of ocean renewable energy which could be developed is about 748GW, and the level of its consumption could reduce up to 5.2 billion tons of CO_2 emission by 2050. Utilization of ocean energy resources will contribute to the world's future sustainable power supply. Although wave energy converters (WECs) extracting energy from the ocean surface are facing issues of both safety and efficiency, they still represent a very remarkable share of the overall global supply in the future. Various forms of WECs have been developed worldwide, though none of them has been stood out as a definitive choice (Ji et al., 2020). From the perspective of marine resources, offshore regions have relatively more abundant and stable wave energy than near shore in most sea areas (Castro and Chiang, 2020; Zheng et al., 2014). Thereby, with the technical progress, floating WECs are becoming a hotspot.

Generally, a floating WEC system consists of floats which react each other to harness energy from the relative motion in between. Compared to fixed ones, it is more flexible as it less affected by water depth and is not limited by the power take-off (PTO) forms. Besides, it is easier to deploy and maintain. For the multi-body form, it leads to multiple resonant characteristic which broadens the operational sea condition. Taking the advantages, many floating WECs have been investigated.

Some devices absorb energy using relative motion of the sealed hull and heavy counterweights inside (Crowley et al., 2018), whose concept amplifies the energy under low frequency and small amplitude waves. One of the representatives is the Wello Penguin, and the full-scale prototype of which has been tested in the European Marine Energy Center (Tethys, 2019). Another WEC under this principle is SEAREV, which utilizes the interaction between the pendular wheel and the hull to produce electricity, and where the centre of gravity of the wheel is off-centred (Cordonnier et al., 2015). The approach of using wave curvature along its propagation direction to extract energy is also considered, and most of which incorporate hydraulic system to convert energy. The raft-type one, such as McCabe Wave Pump, which articulates three rectangular floating pontoons, uses the relative motion in pitch to drive the energy conversion system (Liu et al., 2018). This methodology also underpins the design of Pelamis, whose four rafts move adjacently and drive the hydraulic PTOs to absorb energy (Henderson, 2006).

Although the above novel WECs have been well studied, point absorbers utilizing heave motion for wave energy conversion still occupy a certain proportion in wave energy devices. This kind of WEC typically employs floats to react against each other, to generate mechanical energy which is extracted by means of PTO. Powerbuoy, a cost-effective two-body heaving WEC, utilizes relative motion between a float and a spar with a heave plate to drive the push rod and convert wave energy (Van Rij et al., 2017). Inspired by the Powerbuoy, the U.S. Department of Energy funded Reference Model 3 (Neary et al., 2014). Apart of that, many other two-body heaving WECs with different functions are invented, some of which are connected to the grid (Rusu and Onea, 2017) and some are used to power mobile devices (Dai et al., 2017; Shi et al., 2019). Optimization of size and shape is an important aspect of improving energy capture. Son et al. (2014; 2016) designed a shaped bottom named ’Berkeley Wedge’ to increase the dynamic response. A streamlined submerged body is adopted in Wavebob to achieve greater relative velocity (Windt et al., 2018). A heave plate is presented in Aegir Dynamo to give the steady reference to the floats (Al-Habaibeh et al., 2010). In addition, Martin et al. (2020) investigated cylinder, sphere and plate type floats, giving sequence of the response performances from the best to the worst. Beatty et al. (2015; 2019) compared different shapes of submerged floats on both Response Amplitude Operator (RAO) and PTO summarily.

The dimension of a float, including draught and diameter, also affects its hydrodynamic response (Amiri et al., 2016). Mass ratio between floats has an effect on the energy absorption as well (Liang and Zuo, 2017), which controls the relative motion with PTO together. Aside from the design of the floats, PTO is another vital aspect to WEC. Electromechanical PTO (Castro and Chiang, 2020), linear generator (Tan et al., 2020), hydraulic PTO (Xu et al., 2019) and other different forms of PTO emerge in endlessly. Electromechanical PTO utilizes rack and pinion system combined generator to realize power conversion. The electrical resistance of the generator and the radius of the pinions have an effect on the PTO damping. Some mechanical PTO systems would assemble a variable inertia flywheel to reach the resonance condition. In this case, the rotational inertia and inertia disc radius should be in consideration (Hernández et al., 2017). Linear generators directly link to the wave without any motion transmission, and several key design parameters that will significantly affect the PTO damping coefficient, i.e., the width of the coil and the radius of the central shaft, which in turn affect the energy capture performance. In the hydraulic system, the damping coefficient of hydraulic cylinder and pressure drop determine the PTO damping together. The piston displacement and accumulator define the PTO stiffness (Negandari et al., 2018). In a word, both the magnitudes of PTO damping and PTO stiffness have an influence on the peak value of capture power. What's more, PTO damping also affects the resonance point (Falnes, 1999). Subsequently, different methods are used to find the optimal PTO. Liang and Zuo (2017) found closed-form solutions for both optimal and suboptimal PTO designs. Jin et al. (2019) used a linear frequency domain model to control generator damping and stiffness actively. It is believed that under optimal shape and PTO designs, when wave frequency is within the natural frequencies of the two floats, two-float heaving WEC can produce more power than single-float one. Nevertheless, the passive motion of a WEC under wave excitation could not get an ideal energy efficiency. As the development of control strategy, passive loading, equivalent saturation control and maximum stroke control are applied, providing the possibility of obtaining higher average power (Van den Berg et al., 2011). Multi resonant control and Q-learning algorithm are also introduced to maximize the energy harvesting (Abdelkhalik and Zou, 2019; Anderlini et al., 2018). Generalized analytical phase control conditions (Bubbar and Buckham, 2020) and unlatching control strategy could also increase average energy absorption (Henriques et al., 2012).

This paper focuses on a fundamental study of a two-body heaving WEC under regular waves, seeking the maximum power extraction with optimal PTO damping. The dynamic performance is primarily dependent on the PTO force. Most previous studies have used various methods to apply linear PTO damping force, such as mechanical method (Martin et al., 2020) or linear generator (Tan et al., 2020). Although linear PTO damping is simple and common for analysis, constant PTO force is also another major damping form. Thus, in this paper, the physical model test is conducted to explore the hydrodynamic performance of the WEC, and constant PTO damping force is applied to the model via a specially designed hydraulic control. In numerical simulation part, both linear and non-linear PTO damping forces are determined. The results presented in this paper are all model scale values.

The paper is organized as follows. In Section 2, a two-body heaving WEC physical model test is established, where the constant PTO damping force is introduced in the model test. Section 3 introduces the method of simulation. Section 4 illustrates the comparative analysis of experimental and numerical results, where the simulation model is validated by free decay, RAO and power capture tests. Section 5 discusses the results of the numerical dynamics model, revealing the characteristics of the WEC. Finally, section 6 draws the conclusion of the study, giving methodological comparison and suggestion to the two-body heaving WEC optimization, and expectation of the further work as well.

2 Physical model test

2.1 Model setup

A 1:9 scale model test of the proposed WEC based on the Froude similarity law is conducted in Shandong Provincial Key Laboratory of Ocean Engineering, as shown in Fig. 1. The wave tank is 60 m long, 36 m wide, 1.5 m deep, and features a piston-type wave maker which can generate waves with heights ranging from 0.05 m to 0.25 m, and periods ranging from 0.5 s to 2.5 s in both regular and irregular wave conditions. The tank absorbs wave energy with a sloped porous medium at the end and vertical ones in front of the flanks to minimize the wave reflection. The layout of the wave tank for the physical model test is shown in Fig. 2. The water depth of the physical model test is 1.10 m, and the model is placed 30 m from the wave maker and 7 m from one side of the flanks, so that the wall effect can be ignored.

Wave gauges are used to measure the fluctuation of the water surface. An NDI Optotrack Certus is used to record the motions of the floats. Before the physical model test, all measurements are calibrated. Fig. 3 shows the positions of the wave gauges and the NDI.

The WEC consists of two coaxial floats, which are neutrally buoyant and only have the heave motions. The model set is a non-mooring system. As shown in Fig. 4, the outer float moves along three guide rods (①②③), while the inner one moves along the other two (④⑤). A frame is assembled outside of the model set and fixed to the tank, to make sure the model stays in an upright position. The geometric parameters of the model are given in Table 1 in detail.

In the test, a hydraulic system is applied to provide the PTO damping. As shown in Fig. 5, it controls constant PTO force by adjusting hydraulic pressure. In the hydraulic system, relief valve (6) is used to keep steady pressure and regulate pressure. Solenoid operated directional valve (7) is intended to exhaust gas from the hydraulic circuit. Proportional valve (9) is assembled to control the hydraulic pressure. The error between the PTO force provided by the hydraulic system and the desired value is within 10%, and the error of the period is within 1%. It can be considered that the PTO damping force applied by the hydraulic system can meet the test requirement. More detailed analysis of the PTO force is shown in Section 4.3.

2.2 Regular wave condition

Sea state of North China presents the characteristics of small wave height and short wave period. As one of the most representative sea, Zhaitang Island, has been selected as a marine energy test center in North China. The most frequent occurring wave conditions of this island include the wave heights of 0.25–0.75 m and the wave periods of 3.0–4.0 s (Liu et al., 2017). Considering capacity of the wave tank, and inherent performance of the WEC, the model test selects the conditions with a wave height range between 0.075-0.20 m and a period between 1.05-2.30 s.

3 Numerical model

The numerical model is established using the boundary element method software Ansys-Aqwa to obtain the inviscid hydrodynamic coefficients, such as added mass and radiation damping. Panel methods are used to analyze the hydrodynamic behavior in waves (Fig. 6). The numerical model simulates the hydrostatic restoring force, radiation force and wave excitation force. The additional user-defined viscous force, which is obtained by experimental data, can be optionally included in the equation of motion. Furthermore, the PTO damping force is also imposed through user defined process.

The governing equation of the two-body heaving WEC in frequency domain is,

$$\begin{cases}[-\omega^2(m_1+A_{11}+A_1)+i\omega(B_{11}+B_{vis1})+C_1]Z_1+(-\omega^2A_{12}+i\omega B_{12})Z_2=F_{e1}\\ [-\omega^2(m_2+A_{22}+A_2)+i\omega(B_{22}+B_{vis2})+C_2]Z_2+(-\omega^2A_{21}+i\omega B_{21})Z_1=F_{e2}\end{cases} \quad (1)$$

where, subscript 1 denotes to the outer float, and 2 represents the inner float, respectively; m_i stands for the mass of a float; A_{ij} is the added mass and A_i is the amended added mass; B_{ij} is the radiation damping coefficient; C is the restoring force coefficient; B_{visi} is the linearized viscous damping coefficient; F_{ei} is the complex amplitude of the exciting force on a float which causes its heave motion; Z_i is the complex amplitude of the heave motion of a float.

In frequency domain analysis, PTO damping force is not taken into account, and all the motions are harmonic. The amended added mass and linearized viscous damping coefficients are complemented by free decay test which is discussed in Section 4.1.

The set of dynamic equations describing two floats' heave motions in time domain can be expressed as follows,

$$\begin{cases}[m_1+A_{11}(\infty)+A_1]\ddot{z}_1(t)+A_{12}(\infty)\ddot{z}_2(t)+k_{11}(t)*\dot{z}_1(t)+k_{12}(t)*\dot{z}_2(t)+B_{vis1}\dot{z}_1(t)+C_1z_1(t)=f_{e1}(t)+f_{PTO}(t)\\ [m_2+A_{22}(\infty)+A_2]\ddot{z}_2(t)+A_{21}(\infty)\ddot{z}_1(t)+k_{22}(t)*\dot{z}_2(t)+k_{21}(t)*\dot{z}_1(t)+B_{vis2}\dot{z}_2(t)+C_2z_2(t)=f_{e2}(t)-f_{PTO}(t)\end{cases}$$

(2)

where, f_{ei} is the exciting force on a float which causes its heave motion; $z(t)$ is the heave motion of a float, where $\dot{z}(t)$ and $\ddot{z}(t)$ are the velocity and the acceleration, respectively; the symbol $(*)$ denotes the operation of convolution. f_{PTO} is the PTO damping force. Further, $k_{ij}(t)$ is the radiation-force impulse-response function, which is the inverse Fourier transform of

$$K_{ij}(\omega)=i\omega\left[A_{ij}(\omega)-A_{ij}(\infty)\right]+B_{ij}(\omega) \tag{3}$$

where $A_{ij}(\infty)$ is the added mass when $\omega=\infty$.

In time domain analysis, PTO damping force are calculated at each timestep by user-defined routine. The PTO damping force yields $f_{PTO}=-Bsgn(\dot{z}_1-\dot{z}_2)|\dot{z}_1-\dot{z}_2|^{\frac{1}{n}}$, where B is the damping coefficient, and n is the PTO nonlinear factor. If $n=1$, the PTO force is linear, and if $n\rightarrow\infty$, the PTO force is a Coulomb PTO and its value is constant. In fact, when $n>100$, the nonlinear PTO force can be very close to a constant PTO force, which is shown in Fig. 7. The results of the time domain analysis only remain the steady-state response.

4 Model validation and comparison of numerical and experimental results

In this section, the numerical model is calibrated by heave decay physical model test and validated by regular wave physical model tests. The conditions regarding to the PTO damping force are different in the frequency domain and time domain analyses. For power capture test, the model test only considers the constant PTO damping force, while the time-domain numerical model simulates both linear and nonlinear PTO damping force, including the case of constant PTO damping force.

The frequency-domain numerical model only considers the cases with no PTO. Table 2 lists the differences in these cases.

4.1 Heave decay with no PTO

Free decay test is taken to check the natural periods, and the hydrodynamic coefficients of the model could be determined at these natural periods. Here, the free decay test is carried out in still water for heave motions. The heave decay tests of the two floats are carried out separately. One of the floats is forced to an initial displacement, along the vertical axis, and then is allowed to return naturally to its equilibrium position. During the process, the decay motion of the float is recorded, while the natural period in heave is measured as the period between peaks of the recorded motion. At the same time, the other float keeps at the equilibrium position. In the data analysis, the total added mass a and the damping coefficient b are determined from the exponential decay curve, which are calculated in the following equations (4) and (5).

$$a = \frac{k}{{\omega_0}^2} - m \tag{4}$$

$$b = \frac{2C\xi}{\omega_0} \tag{5}$$

where $\omega_0 = \frac{2\pi}{T}$ is the natural frequency of oscillation, C is the restoring force coefficient, m is the mass of a float and ξ is the damping ratio.

Based on the decay test data of the physical model and the hydrodynamic coefficients calculated by the software, numerical model is calibrated by modifying the amended added mass and the linearized viscous damping coefficient to match the real motion of the floats considering the viscous effects. Fig. 8 shows the results of a free oscillation test in heave of the two floating bodies. The decay curves from the experimental and numerical results are quite close. As shown in Fig. 8, the natural period of the outer float is approximately 1.29 s whereas the natural period of the inner one is approximately 1.82 s.

4.2 Heave motion RAO with no PTO in regular waves

Regular wave test without the influence of PTO is undertaken to obtain the heave motion RAO and to assess the validity of the numerical simulation modified by free-decay test as discussed in Section 4.1. Without the experimental data, the heave motion RAO of this system will be heavily over-predicted. The model tests are performed with two floating bodies coupled. The heave motion RAO, which is defined as the amplitude of the body's heave motion, normalized by the wave amplitude, and also regarded as a function of wave period, is used to evaluate the hydrodynamic performance of the two-body heaving WEC. The experimental RAOs are obtained from regular wave tests without PTO damping force. The ratio between heave motion response and wave signals is obtained over a range of wave periods under regular wave conditions. Noting that, the numerical results conduct two simulation results in frequency and time domain, respectively.

Experimental and numerical heave motion RAOs of the two bodies without PTO damping force are plotted in Fig. 9, which are in good agreement. Fig. 9(a) shows that the outer float has a good wave following property in most periods. The responses have a great promotion from 1.05 s to 1.30 s, and remain approximately 1.0 afterwards. Fig. 9(b) reveals that the inner float is more sensitive to the wave period than the outer one, which has an obvious resonance range. That may be due to the streamline shape of the float. At 1.80 s, the resonance condition is approached where the heave displacement amplitude is three times of the incident wave. The relative heave motion RAO is defined as the ratio of the amplitude of the instantaneous relative movement of the outer and inner floats to the wave amplitude, which is shown in Fig. 9(c). It also obtains the peak value at the period of 1.80 s. Since the outer float has no distinct peak value of RAO, the relative motion appears to have a similar tendency to that of the inner float. When the wave period is small, the inner float has a weak response, and the performance of the system mainly depends on the response of the outer one. As the period increases to the resonance range of the inner float, it interacts strongly with wave, which leads to a large relative motion. When the wave period continues increasing, the motions of two floats tend to be consistent, and the relative motion is reduced. Regardless of large wave periods, the relative motion has a better performance than any of the two single floats, especially when the period is small. The opposite phenomenon occurs under large wave periods.

In summary, the two-body heaving WEC has better response than a single-body one under shorter wave periods, the motion characteristics of the outer and inner floats are mixed to supply a greater contribution to the united system. The heave motion RAO curves show that this model is suitable for the selected sea state with the outer float as the absorber. The numerical model is valid under free oscillation when supplied with experimentally derived added mass and damping coefficients.

4.3 PTO force and relative float motion in regular waves

The cases of constant PTO damping force supplied by the hydraulic system in physical model test are taken into account. Fig. 10(a) and (b) illustrate the comparisons of the changes of PTO damping force with time and with relative motion. The data are recorded from time domain numerical model and physical model test. Time series of relative motion is shown in Fig. 10(c). Numerical results are more stable and higher than experimental ones, but the periodicity is good. Fig. 10(d) and (e) show the comparisons of the amplitudes of PTO damping force, relative motion and relative velocity between physical model test and time domain simulation results under two regular wave cases with T=1.30 s, H=0.175 m (case 1) and H=0.20 m (case 2), respectively. The trends of curves between them are quite similar. PTO damping force is measured by pressure sensor in physical model test, while the numerical model results are the configured values. As shown in Fig. 10, the PTO damping force applied to the WEC in the physical model test is relatively smaller compared to the numerical model. However, focusing on WEC relative motion and relative velocity, numerical results perform better than experimental ones. That may cause by the friction loss of the hydraulic system. The PTO damping force applied in the model test is obtained by multiplying the pressure difference of the hydraulic cylinder by the cavity area, ignoring the friction of the hydraulic system. Therefore, the measured PTO damping force in the physical model test is less than the actual damping force applied to the floats and the relative motion is smaller than numerical ones. It is believed that in the full-scale model, the proportion of friction loss is small, so that it is not taken into account in the following numerical model. In Fig. 10(f) and (g), the comparisons of capture width ratio (CWR) under case 1 and 2 are investigated, which are the combination of PTO force and relative motion (shown in Fig. 10(d) and (e)). There is a certain difference in absolute values, but the trends of the curve are consistent.

For more proof, the comparisons of the optimal coefficient between physical model test and time domain simulation are illustrated in Fig. 10(h). In addition to case 1 and 2, case 3 (T=1.55 s, H=0.175 m) and case 4 (T=1.55 s, H=0.20 m) are added for comparison. It can be seen that there is a good match between the physical and simulation model in terms of the optimal coefficient. It can also be proved that the constant PTO damping force can be applied in the numerical simulation.

Based on the above discussions, the numerical dynamics model agrees well with experimental results in terms of displacements, RAO, PTO force and power capture. The numerical dynamics model is considered to be valid for the purposes of this study. To further explore the properties of WEC, the below part is discussed by simulation model data. What's more, in order to show the performance in more detail, the simulation extends the wave conditions to the wave height between 0.05-0.08 m and the wave period between 0.80-2.60 s.

5 Power capture performance with different PTOs for regular wave conditions

Sensitivity study of power capture performance of the two-body heaving WEC is conducted in this section using time-domain numerical simulation models. Power capture performance under different PTO models, wave heights and periods are compared. Phase angle between different PTO damping forces are also contrasted. All of the analyses are based on the time domain simulation results. Nondimensional numbers are suggested to obtain the laws of performance for upscaled WEC. Table 3 shows the dimensional and the corresponding nondimensional quantities used in this section.

5.1 Power capture performance for different wave heights

Data from time domain model results with constant PTO damping are given in Fig. 11. The wave heights are H=0.10-0.20 m, with the interval of 0.02 m, and T=1.40 s. The data plotted are mechanical power capture and CWR as a function of PTO damping force. The energy captured is calculated by multiplying PTO damping with relative motion during the time history. As shown in Fig. 11(a), the higher wave height is, the more power produces. The optimal PTO damping force increase with the increase of the wave height. Meanwhile, the CWR is also proportional to the wave height, as shown in Fig. 11(b). Normalize the PTO damping force by $\rho g D^2 H$, where ρ is wave density, g is gravitational acceleration, D is the diameter of the outer float and H is the wave height. For one certain wave period, the curve of mean power is consistent with the change of normalized force under various wave heights. In respect of linear PTO damping force condition, the mean power and its corresponding CWR increase first and then decrease, along with the increase of damping coefficient, as shown in Fig. 12. The captured power is proportional to the wave height, while the curves of CWR at different wave heights are coincident. In contrast to constant PTO force, the optimal PTO damping coefficient is fixed for one wave period. What's more, the energy acquisition of the device under linear damping is more moderate with the change of damping coefficient.

5.2 Optimal PTO damping coefficients for the two-body heaving WEC

The curves of optimal coefficients of PTO damping force, which is defined as the corresponding damping coefficient when the maximum energy is reached at certain period, are shown in Fig. 13. For constant damping force, as seen in Fig. 13(a) and (b), the optimal coefficient goes up to a peak value and subsequently declines with the increase of wave period. In particular, the optimal damping coefficient reaches the maximum value under the optimal capture wave period. Obviously, higher wave heights will have larger optimal coefficient. When the optimal coefficient normalized by $\rho g D^2 H$, it only depends on the wave period. Accordingly, the optimal coefficient of constant damping is proportional to wave height. Fig. 13(c) and (d) show that the optimal damping coefficient of linear PTO damping force decreases first with respect to wave period and normalized wave period, and then increases again when the period gets to the synchronous motion of the two floats. Wave height has no effect on the optimal coefficient under linear PTO damping force. It can be seen that the optimized damping coefficients can be so different under different periods.

The characteristics of optimal damping and power capture are so different due to hydrodynamic properties, as expected. For constant PTO damping force, both wave height and period affect the power capture and optimal coefficient, whereas linear damping, only wave period does.

5.3 Sensitivity study for regular wave conditions

When the PTO damping coefficient is fixed, constant PTO damping force exhibits different capacities under different wave height, while linear PTO damping force remains consistent, as shown in Fig. 14. This is because, as discussed above, the optimal coefficient that can be obtained at different wave heights are different with constant PTO damping force, and in regard to linear system, only the incident wave period matters.

Observing from Fig. 9(c), the peak value of relative heave motion RAO appears at 1.80 s. However, the high relative motion amplitude is associated with low power production, as shown in Fig. 14(a) and (c). Therefore, blindly increasing the relative motion does not improve energy production. Due to the influence of PTO damping force, the maximum response interval of the system changes, moving towards the shorter wave periods. The results of the model show that the system has a good power capacity under small wave periods between 1.40-1.60 s, that is, between the resonance periods of the two bodies. The ability of power capture gets worse when wave period exceeds the optimal range, and synchronism occurs.

The power capture performance with different constant PTO damping force varies with the wave height. Observing the curves of mean power in Fig. 15(a), as the PTO damping rising, the curvature of energy growth ascends. For its corresponding CWR, as shown in Fig. 15(b), CWR falls down with the increase of the wave height under small constant PTO damping force, then as the force increases, the degree of decrease becomes slower and turns to an upward tendency, and from the convex curve to concave curve, gradually. Therefore, in the power capture range, as the constant PTO force goes up, the energy obtained will ascend at a faster rate as the wave height goes up. Differ from constant force, wave height improves the mean power capture monotonically under linear damping, while the corresponding CWR does not change, as shown in Fig. 15(c) and (d).

5.4 Power capture performance with different PTO models

The comparisons of optimal mean power capture as a function of wave period between constant and linear PTO forces are shown in Fig. 16. When the wave period is shorter than 1.80 s, the resonance period of the inner float, linear PTO damping force are better than the constant one. When the period exceeds 1.80 s, the difference is very tiny. Wave height has no impact on the optimal power. For CWR comparison, wave height has no influence on the maximum power capture.

As introduced in Section 3, the PTO damping force yields $f_{PTO} = -Bsgn(\dot{z}_1 - \dot{z}_2)|\dot{z}_1 - \dot{z}_2|^{\frac{1}{n}}$. The PTO nonlinear factor n is introduced to evaluate power capacity, which is used to characterize the nonlinearity of PTO damping force. In order to better display in the figure, here, assuming that the PTO nonlinear factor of constant PTO damping force is 150. As shown in Fig. 17, the maximum power increases first and then drops down with the increase of n, and reaches the maximum when $n = 1$, that is, the linear damping. In this comparative analysis, the PTO damping coefficient is set to an optimized value that is specific to each PTO and wave conditions. It indicates that the linear damping is the optimal PTO damping form to this system.

Contour plots of mean power production and CWR as a function of H and T for constant and linear PTO damping forces are shown in Fig. 18. The optimum passive PTO damping force was chosen for each wave condition. Linear PTO damping force has a better power capture performance than constant force under the same sea state, but with very litter difference. In that sense, changing the type of PTO damping force can only improve the capacity to a limited extent. The main power band is concentrated between the heave natural periods of the two bodies. Wave period corresponding to the peak value of the mean power is longer than the period corresponding to the peak value of CWR.

5.5 Phase angle with different PTO models

The phase angle is used to describe the phase difference between the outer and the inner floats. The phase angle is larger in the absence of PTO forces than that in the presence of PTO force. The maximum phase angle without PTO force is 125° at 1.60 s, and approximately zero phase angle above 2.0 s. As shown in Fig. 19, it is very difficult to make these two bodies move in opposite direction under passive damping. They get a maximum phase angle at 1.80 s, which is the natural period of the inner float. The PTO damping force reduces phase angle by 55%. When the wave period exceeds 1.80 s, the phase angle plunged to zero.

6 Conclusions

In this paper, a 1:9 scaled model of a two-body heaving WEC is studied both experimentally and numerically, with focus on the power absorption performance and the motion characteristics of the WEC. The linearized viscous damping coefficients derived from the physical decay model test is used to calibrate the numerical model to achieve a good comparison to the experimental results. The numerical result under regular wave condition has a good agreement with that of the physical model test. Sensitive study of this system is conducted using the validated time-domain numerical models, and the conclusion that larger relative movement does not mean better power capture is drawn. Linear PTO damping system is more suitable for this system with consideration of the PTO nonlinear factor n. For the different wave heights that were considered in this study, the WEC system behaves linearly.

The hydrodynamic performance of this system depends on the coupling property of the two floats and has a decent motion response in resonance range. The power production is markedly affected by the wave period. Phase angle between the two floats is not the only indicator of power capacity. In terms of power capture, the system has a good performance when the wave period is between the two floats' natural periods and especially at the average value of their natural periods. As a result, a larger separation between two natural periods is beneficial, leading to a wider and higher capture band.

The paper addresses the dynamic performance of the two-body WEC, with no active phase control, which will be applied in the future.

Acknowledgments

This work was supported by the National Key R&D Program of China (Grant No.: 2018YFB1501904), Shandong Provincial Key R&D Program (Grant NO.: 2019JZZY010902), China Scholarship Council, and the National Natural Science Foundation of China (Grant No.: 52071303, 41376100).

References

Abdelkhalik, O., Zou, S., 2019. Control of small two-body heaving wave energy converters for ocean measurement applications. Renew. Energy 132, 587-595. https://doi.org/10.1016/j.renene.2018.08.004.

Al-Habaibeh, A., Su, D., McCague, J., Knight, A., 2010. An innovative approach for energy generation from waves. Energy Conversion and Management 51 (8), 1664-1668. https://doi.org/10.1016/j.enconman.2009.11.041.

Amiri, A., Panahi, R., Radfar, S., 2016. Parametric study of two-body floating-point wave absorber. J. Mar. Sci. Appl. 15 (1), 41-49. https://doi.org/10.1007/s11804-016-1342-1.

Anderlini, E., Forehand, D.I.M., Bannon, E., Xiao, Q., Abusara, M., 2018. Reactive control of a two-body point absorber using reinforcement learning. Ocean. Eng. 148, 650-658. https://doi.org/10.1016/j.oceaneng.2017.08.017.

Beatty, S.J., Bocking, B., Bubbar, K., Buckham, B.J., Wild, P., 2019. Experimental and numerical comparisons of self-reacting point absorber wave energy converters in irregular waves. Ocean. Eng. 173, 716-731. https://doi.org/10.1016/j.oceaneng.2019.01.034.

Beatty, S.J., Hall, M., Buckham, B.J., Wild, P., Bocking, B., 2015. Experimental and numerical comparisons of self-reacting point absorber wave energy converters in regular waves. Ocean. Eng. 104, 370-386. http://dx.doi.org/10.1016/j.oceaneng.2015.05.027.

Bubbar, K., Buckham, B., 2020. On establishing generalized analytical phase control conditions in two body self-reacting point absorber wave energy converters. Ocean. Eng. 197. https://doi.org/10.1016/j.oceaneng.2019.106879.

Castro, F.A., Chiang, L.E., 2020. Design optimization and experimental validation of a two-body Wave Energy Converter with adjustable Power Take-Off parameters. Energy for Sustainable Development 56, 19-32. https://doi.org/10.1016/j.esd.2020.02.007.

Cordonnier, J., Gorintin, F., De Cagny, A., Clement, A.H., Babarit, A., 2015. SEAREV: Case study of the development of a wave energy converter. Renew. Energy 80, 40-52. https://doi.org/10.1016/j.renene.2015.01.061.

Crowley, S., Porter, R., Taunton, D.J., Wilson, P.A., 2018. Modelling of the WITT wave energy converter. Renew. Energy 115, 159-174. https://doi.org/10.1016/j.renene.2017.08.004.

Dai, Y.M., Chen, Y.Z., Xie, L.H., 2017. A study on a novel two-body floating wave energy converter. Ocean. Eng. 130, 407-416. http://dx.doi.org/10.1016/j.oceaneng.2016.11.049.

Falnes J. 1999. Wave-energy conversion through relative motion between two single-mode oscillating bodies. J Offshore Mech Arctic Eng. 121:32–38. https://doi.org/10.1115/1.2829552.

Henderson, R., 2006. Design, simulation, and testing of a novel hydraulic power take-off system for the Pelamis wave energy converter. Ocean. Eng. 31 (2), 271-283. https://doi.org/10.1016/j.renene.2005.08.021.

Henriques, J.C.C., Lopes, M.F.P., Gomes, R.P.F., Gato, L.M.C., Falcao, A.F.O., 2012. On the annual wave energy absorption by two-body heaving WECs with latching control. Renew. Energy 45, 31-40. https://doi.org/10.1016/j.renene.2012.01.102.

Hernández, F., Chiang, L. E., & Corbalán, P. (2017). A general architecture for electric powermanagement of small scale NCRE converters: Design methodology and validation. Energy for Sustain. Development, Vol., 41, 128–138. https://doi.org/10.1016/j.esd.2017.09.001.

Ji, X.Y., Al Shami, E., Monty, J., Wang, X., 2020. Modelling of linear and non-linear two-body wave energy converters under regular and irregular wave conditions. Renew. Energy 147, 487-501. https://doi.org/10.1016/j.renene.2019.09.010.

Jin, P., Zhou, B.Z., Goteman, M., Chen, Z.F., Zhang, L., 2019. Performance optimization of a coaxial-cylinder wave energy converter. Energy 174, 450-459. https://doi.org/10.1016/j.energy.2019.02.189.

Liang, C.W., Zuo, L., 2017. On the dynamics and design of a two-body wave energy converter. Renew. Energy 101, 265-274. http://dx.doi.org/10.1016/j.renene.2016.08.059.

Liu, C., Yang, Q., Bao, G., 2018. Influence of hydraulic power take-off unit parameters on power capture ability of a two-raft-type wave energy converter. Ocean. Eng. 150, 69-80. https://doi.org/10.1016/j.oceaneng.2017.12.063.

Liu, Z., Qu, N., Shi, H.D., 2017. Experimental study on hydrodynamic performance of a wave energy converter within multi-heaving-buoys. International J. Energy Res. 41 (9), 1351-1366. https://doi.org/10.1002/er.3725.

Martin, D., Li, X.F., Chen, C.A., Thiagarajan, K., Ngo, K., Parker, R., Zuo, L., 2020. Numerical analysis and wave tank validation on the optimal design of a two-body wave energy converter. Renew. Energy 145, 632-641. https://doi.org/10.1016/j.renene.2019.05.109.

Neary, V.S., Lawson, M., Previsic, M., Copping, A., Hallett, K.C., LaBonte, A., Rieks, J., Murray, D., 2014. Methodology for Design and Economic Analysis of Marine Energy Conversion (MEC) Technologies. Sandia National Lab.(SNL-NM), Albuquerque, NM (United States).

Negandari, M., Dalayeli, H., Moghadas, M.H., 2018. Design of a Two-Body Wave Energy Converter by Incorporating the Effect of Hydraulic Power Take-Off Parameters. Journal of Marine Science and Technology-Taiwan 26 (4), 496-507. https://doi.org/ 10.6119/JMST.201808_26(4).0003.

Ocean Energy System. 2018. Spotlight on ocean energy.

Rusu, L., Onea, F., 2017. The performance of some state-of-the-art wave energy converters in locations with the worldwide highest wave power. Renew. Sustain. Energy Rev. 75, 1348-1362. https://doi.org/10.1016/j.rser.2016.11.123.

Shi, H.D., Dong, X.C., Feng, L., Han, Z., 2019. Experimental Study on the Hydrodynamic Performance of a Heaving Buoy Assembled on a Net Cage Platform. J. Ocean Univ. China 18 (5), 1031-1040. https://doi.org/10.1007/s11802-019-4028-x.

Son, D., Belissen, V., Yeung, R.W., 2016. Performance validation and optimization of a dual coaxial-cylinder ocean-wave energy extractor. Renew. Energy 92, 192-201. https://doi.org/10.1016/j.renene.2016.01.032.

Son, D., Yeung, R.W., 2014. Performance Predictions and Validation of a Two Coaxial-Cylinder System as a Wave-Energy Extractor. 33rd International Conference on Ocean, Offshore and Arctic Eng., 2014, Vol 7.

Tan, Y.M., Liu, N., Lin, K.J., Zhang, Z.G., 2020. Frequency Domain Modeling of a Halbach PM Linear Generator Based Two-Body Point Absorber for Wave Energy Conversion. Front. Energy Res. 8. https://doi.org/10.3389/fenrg.2020.00019.

Tethys, 2019. Wello Penguin at EMEC. https://tethys.pnnl.gov/annex-iv-sites/wello-penguin-emec (Accessed 23 July 2020)

Van den Berg, J., Ricci, P., Touzon, I., Villate, J.L., Tedeschi, E., 2011. Control strategies for improving power performance of two-body heaving wave energy devices, The Twenty-first International Offshore and Polar Engineering Conference. International Society of Offshore and Polar Engineers.

Van Rij, J., Yu, Y.-H., Edwards, K., Mekhiche, M., 2017. Ocean power technology design optimization. International Journal of Marine Energy 20, 97-108. https://doi.org/10.1016/j.ijome.2017.07.010.

Windt, C., Davidson, J., Ringwood, J.V., 2018. High-fidelity numerical modelling of ocean wave energy systems: A review of computational fluid dynamics-based numerical wave tanks. Renew. Sustain. Energy Rev. 93, 610-630. https://doi.org/10.1016/j.rser.2018.05.020.

Xu, Q.L., Li, Y., Yu, Y.H., Ding, B.Y., Jiang, Z.Y., Lin, Z.L., Cazzolato, B., 2019. Experimental and numerical investigations of a two-body floating-point absorber wave energy converter in regular waves. Journal of Fluids and Structures 91. https://doi.org/10.1016/j.jfluidstructs.2019.03.006.

Zheng, C.W., Zhou, L., Jia, B.K., Pan, J., Li, X., 2014. Wave characteristic analysis and wave energy resource evaluation in the China Sea. Journal of Renew. and Sustain. Energy 6 (4). http://dx.doi.org/10.1063/1.4885842.

Fig. 1. Scale model in wave tank.

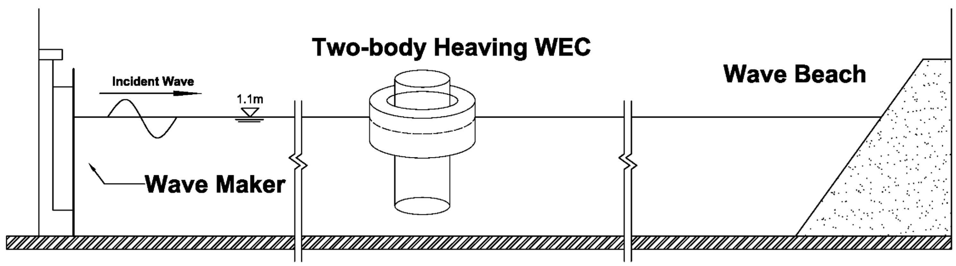

Fig. 2. Wave tank layout for the model test.

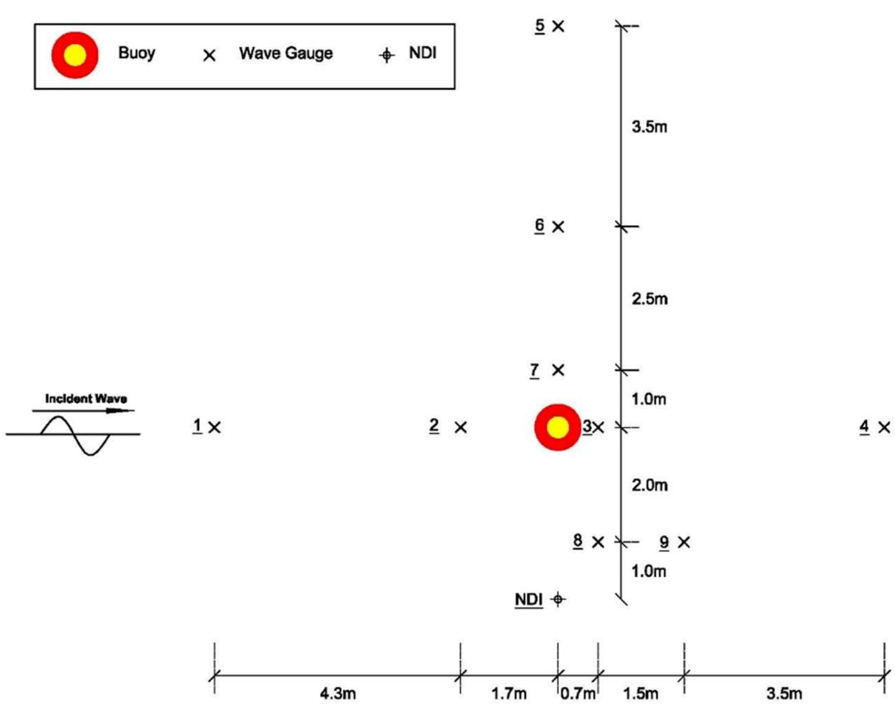

Fig. 3. The deployment of wave gauges and NDI.

Fig. 4. The two-body heaving WEC.

Fig. 5. (a) The hydraulic station.

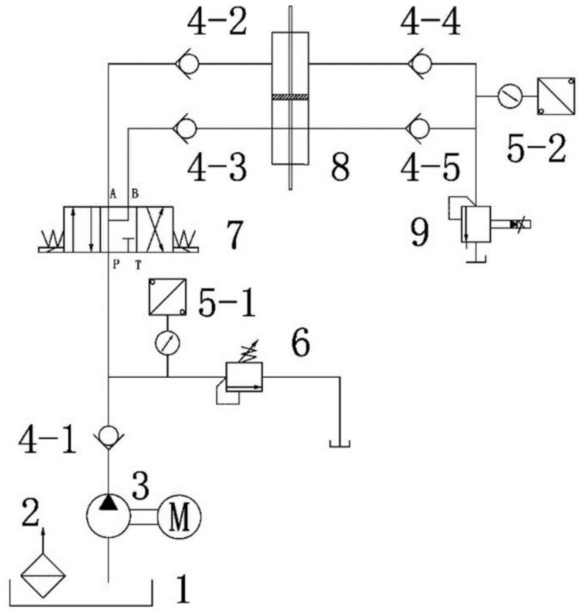

Fig. 5. (b) Schematic diagram of the hydraulic system.

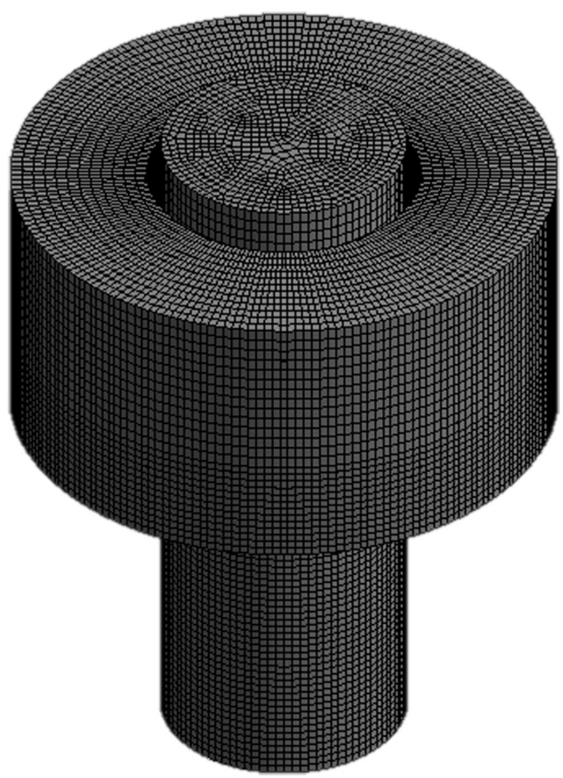

Fig. 6. The mesh used to simulate the heaving two-body WEC.

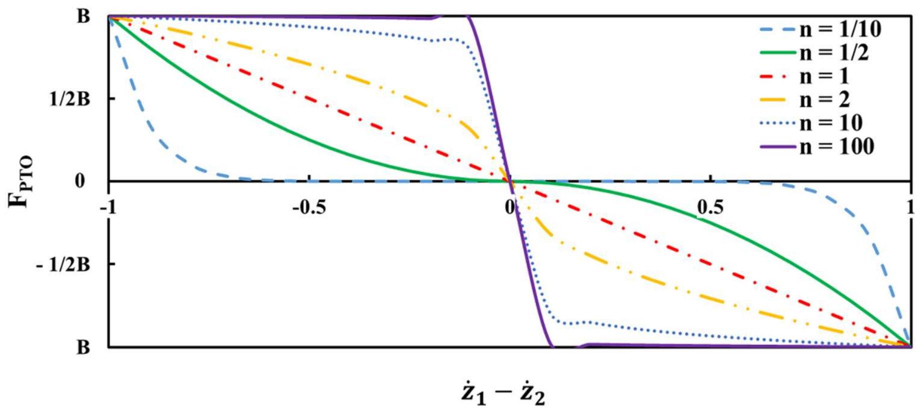

Fig. 7. Nonlinear PTO force for different n.

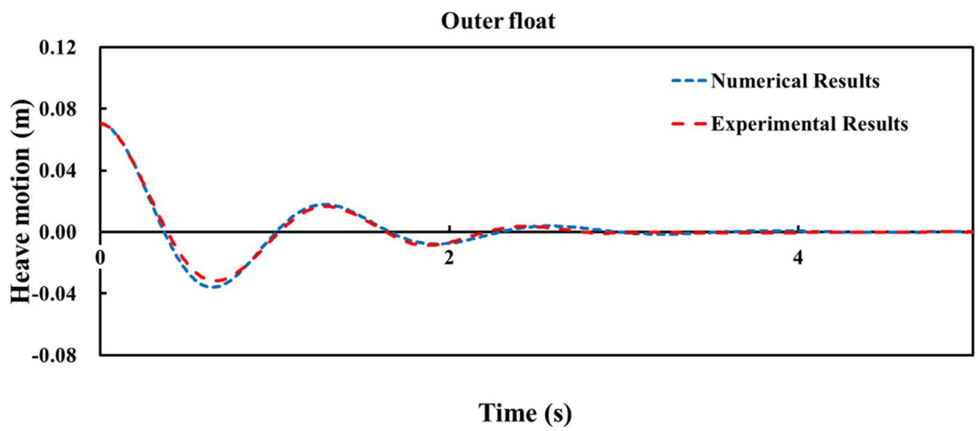

Fig. 8. (a) Heave decay curves of the outer float.

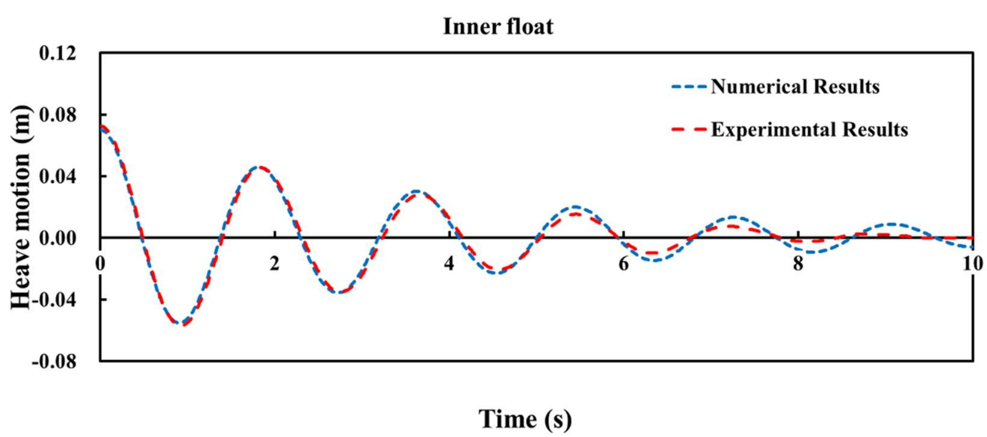

Fig. 8. (b) Heave decay curves of the inner float.

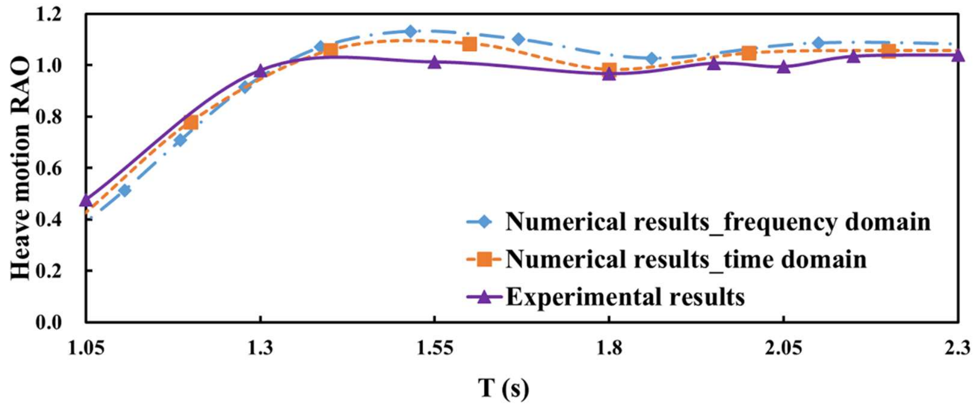

Fig. 9. (a) Heave motion RAO of the outer float.

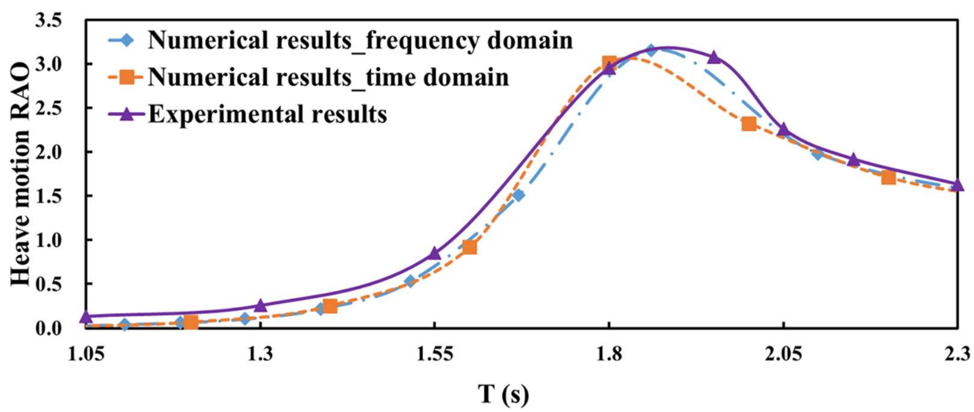

Fig. 9. (b) Heave motion RAO of the inner float.

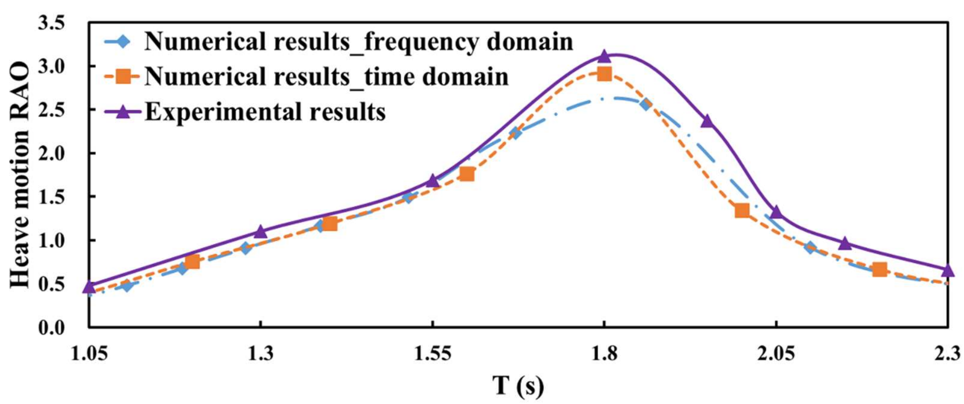

Fig. 9. (c) Relative heave motion RAO.

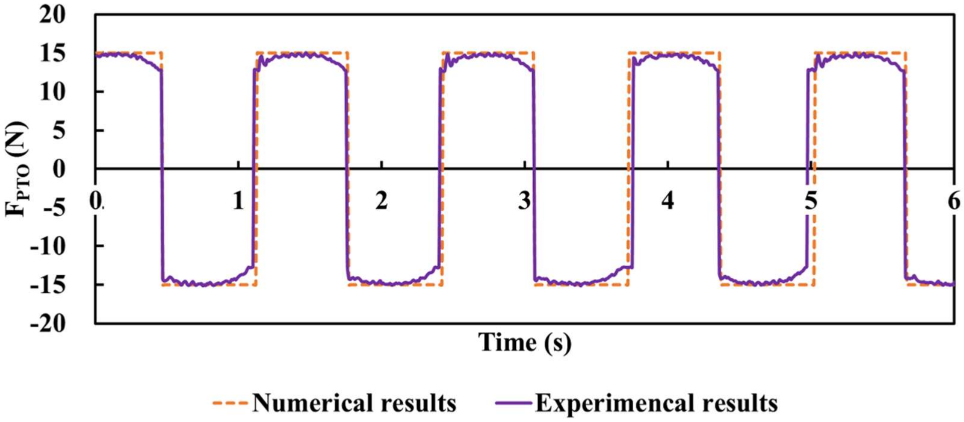

Fig. 10. (a) Constant PTO damping force time series.

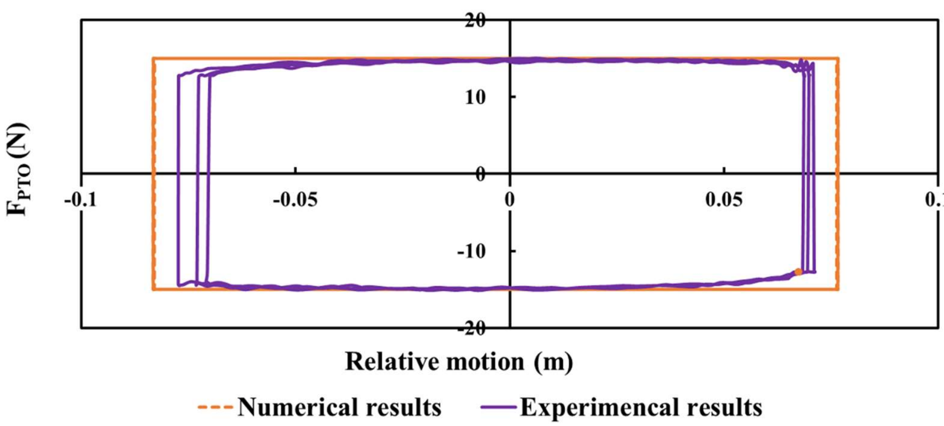

Fig. 10. (b) Constant PTO damping force as a function of the relative heave motion.

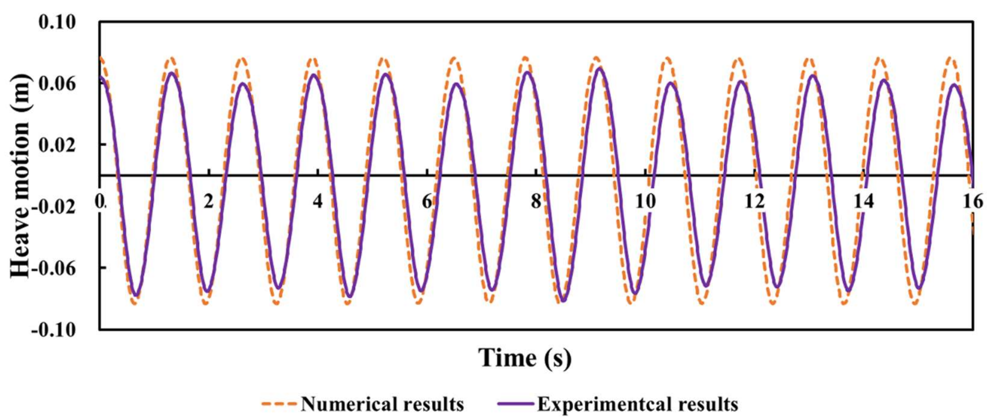

Fig. 10. (c) Relative motion time series.

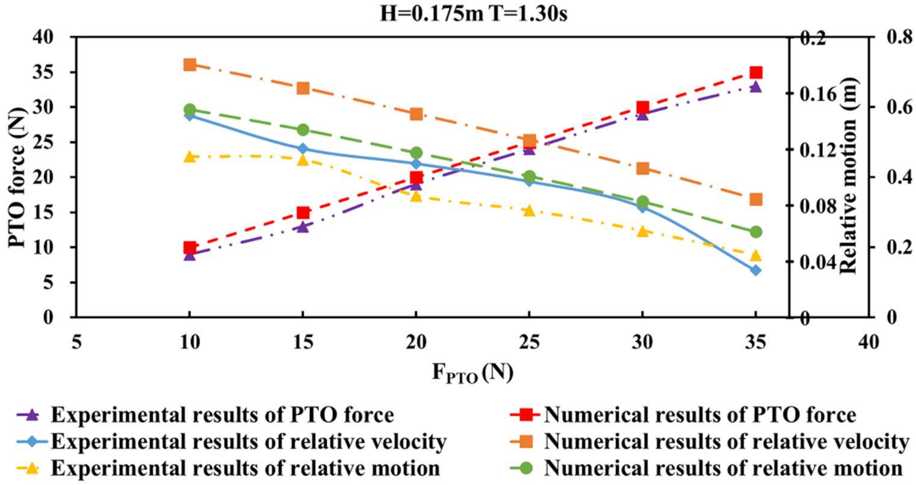

Fig. 10. (d) The comparison of experimental and numerical results under case 1.

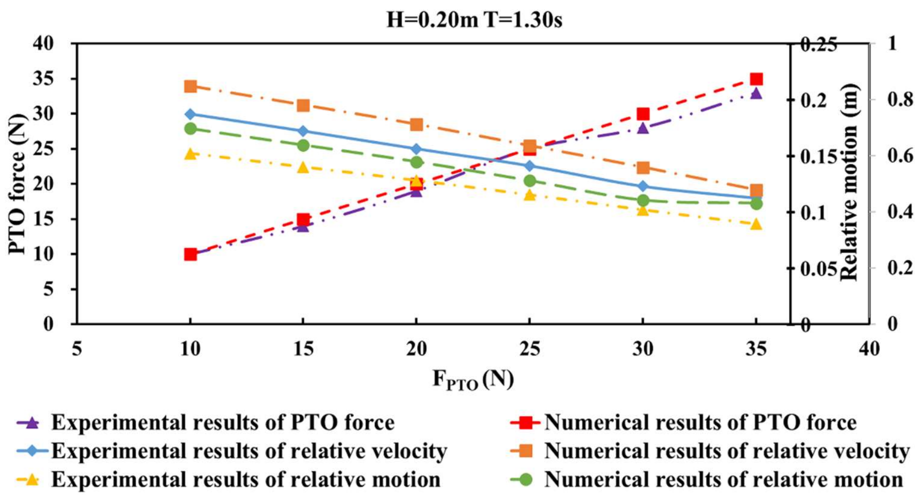

Fig. 10. (e) The comparison of experimental and numerical results under case 2.

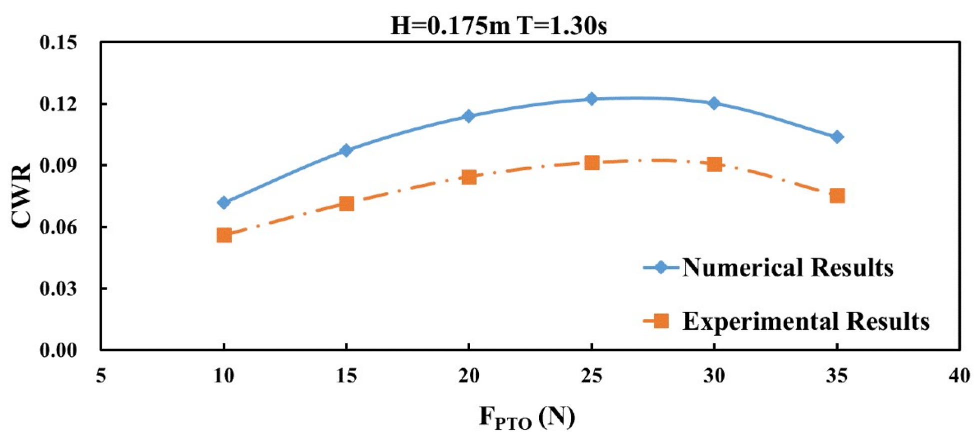

Fig. 10. (f) CWRs of experimental and numerical results under case 1.

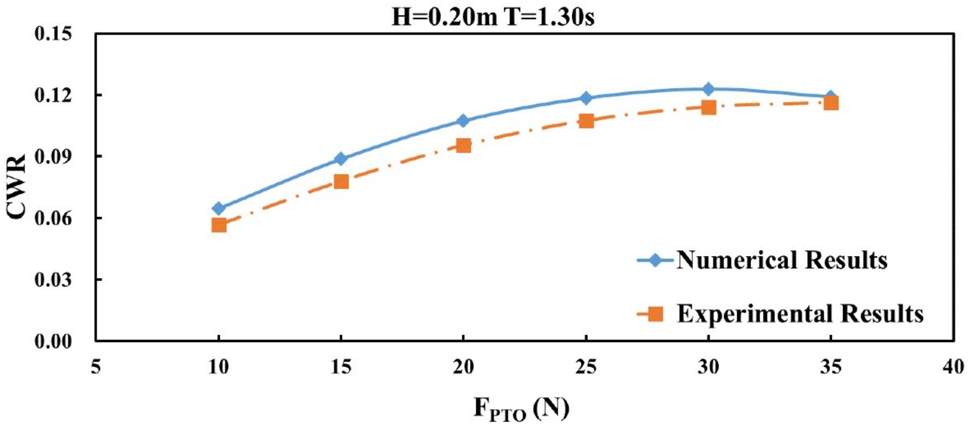

Fig. 10. (g) CWRs of experimental and numerical results under case 2.

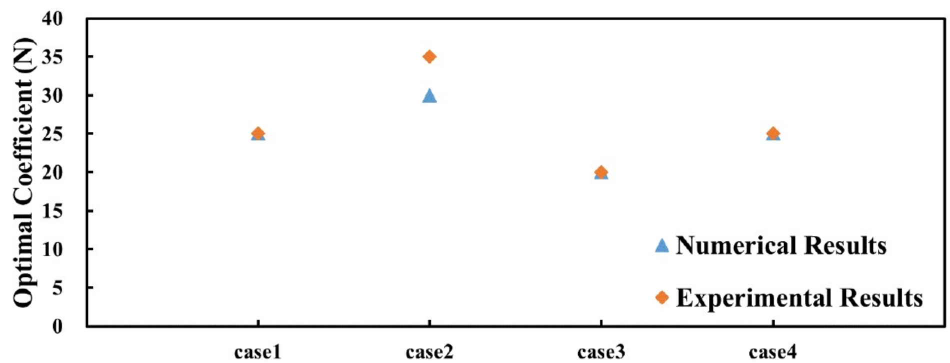

Fig. 10. (h) Optimal coefficient.

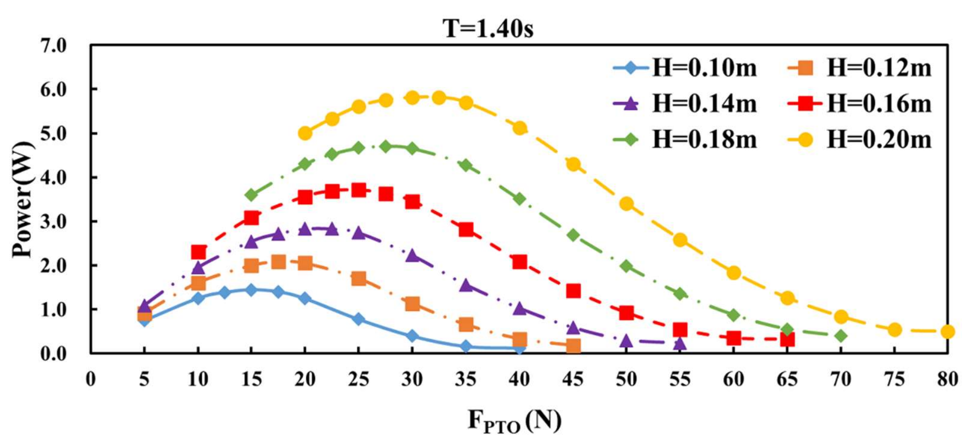

Fig. 11. (a) Mean power as a function of constant PTO damping force.

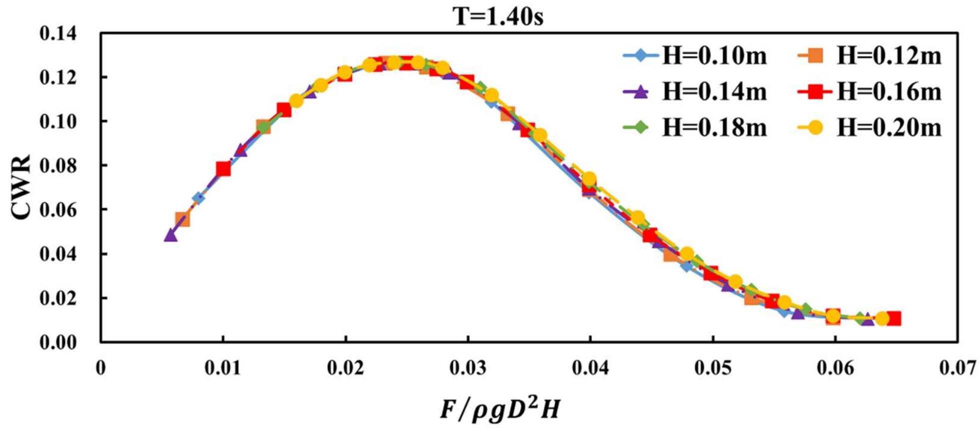

Fig. 11. (b) CWR as a function of normalized constant PTO damping force.

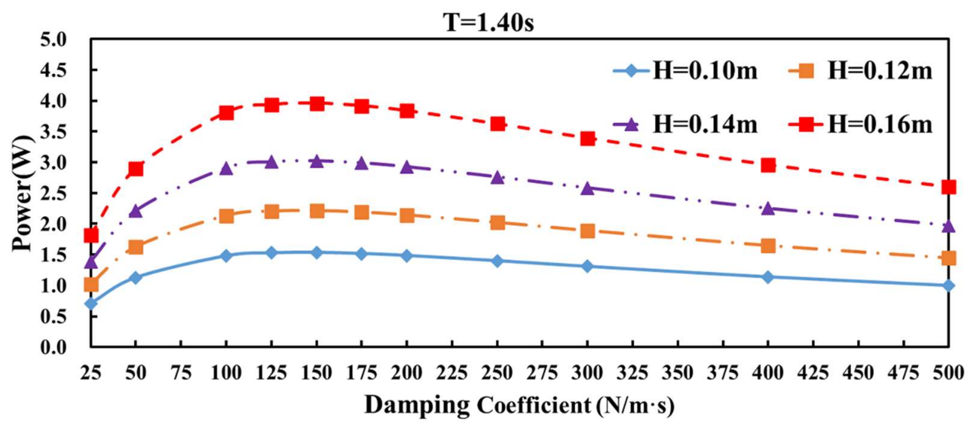

Fig. 12. (a) Mean power as a function of linear PTO damping force.

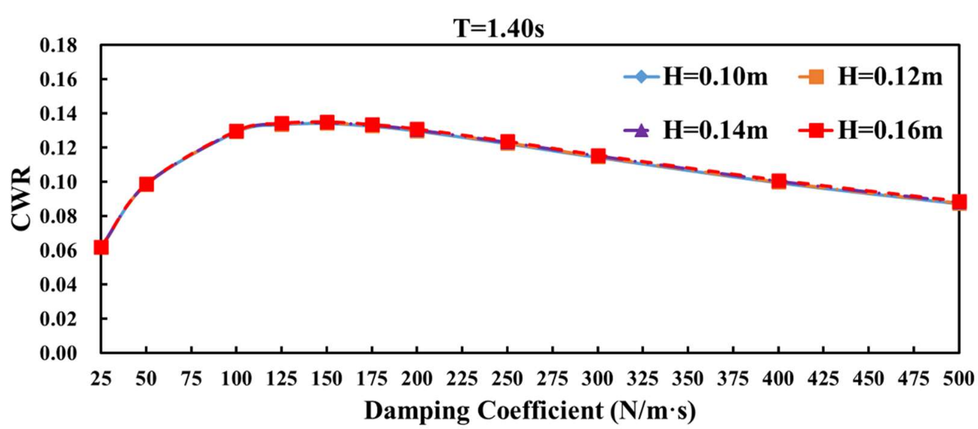

Fig. 12. (b) CWR as a function of linear PTO damping force.

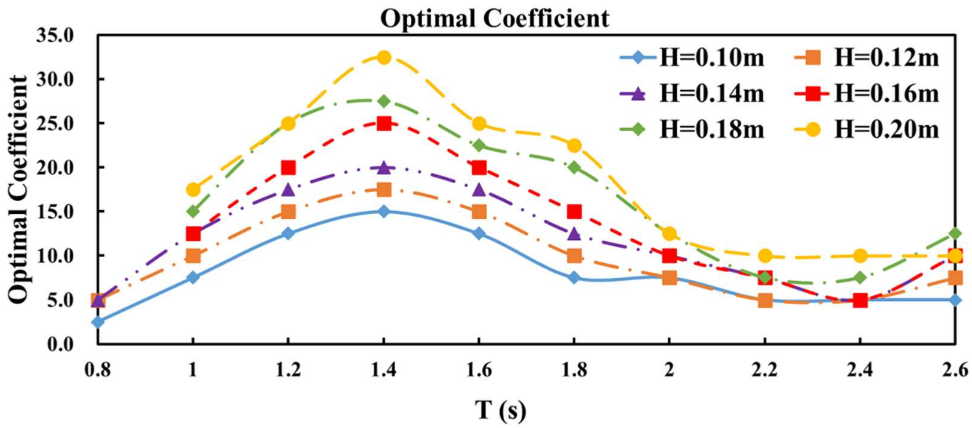

Fig. 13. (a) Optimal coefficient under constant PTO force.

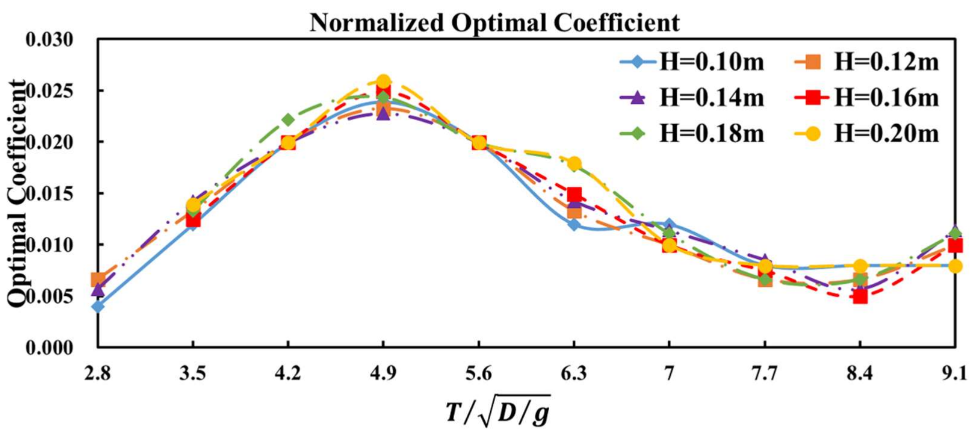

Fig. 13. (b) Normalized optimal coefficient under constant PTO force.

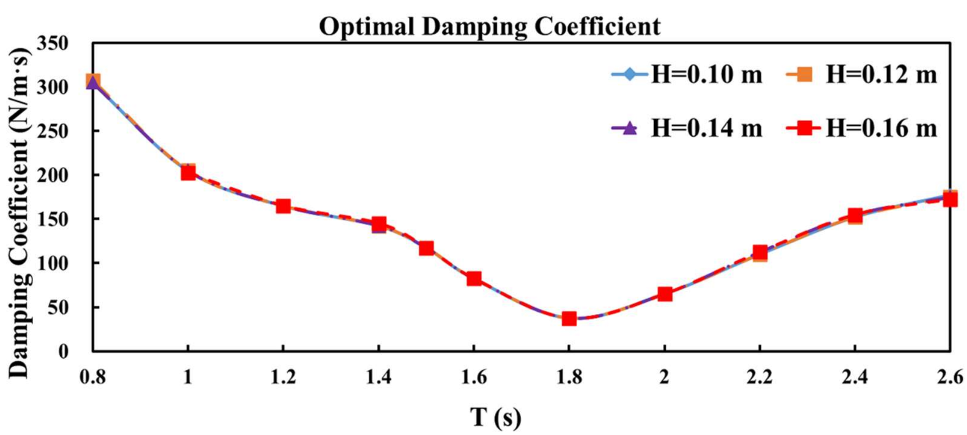

Fig. 13. (c) Optimal coefficient under linear PTO force.

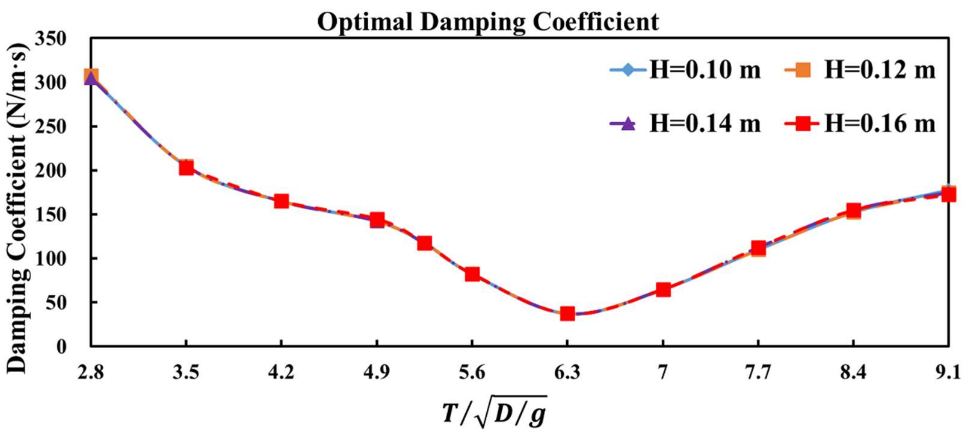

Fig. 13. (d) Optimal coefficient under linear PTO force.

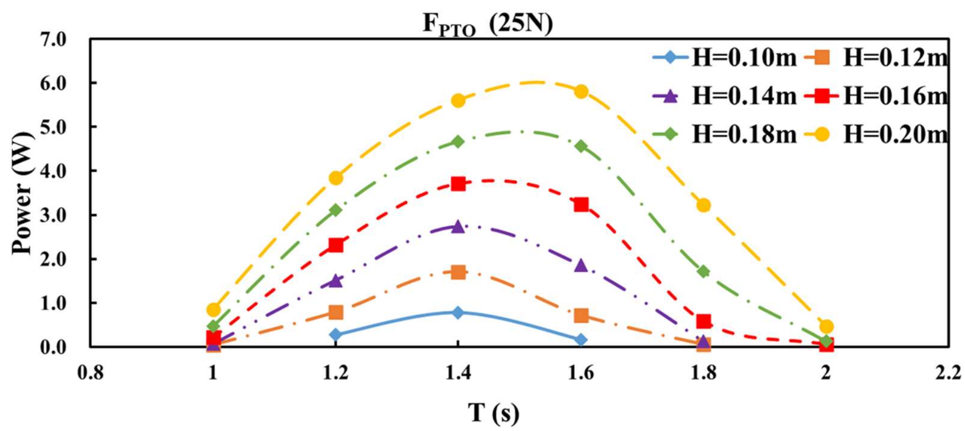

Fig. 14. (a) Capture power under constant PTO damping force.

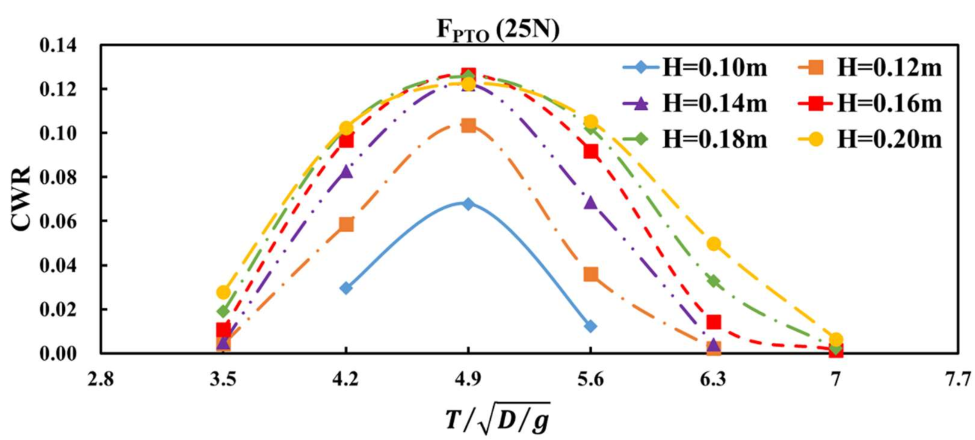

Fig. 14. (b) CWR under constant PTO damping force.

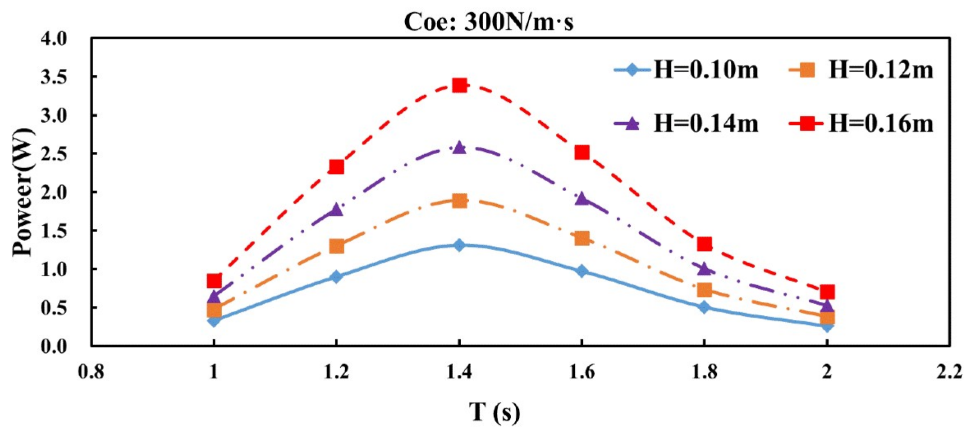

Fig. 14. (c) Capture power under linear PTO damping force.

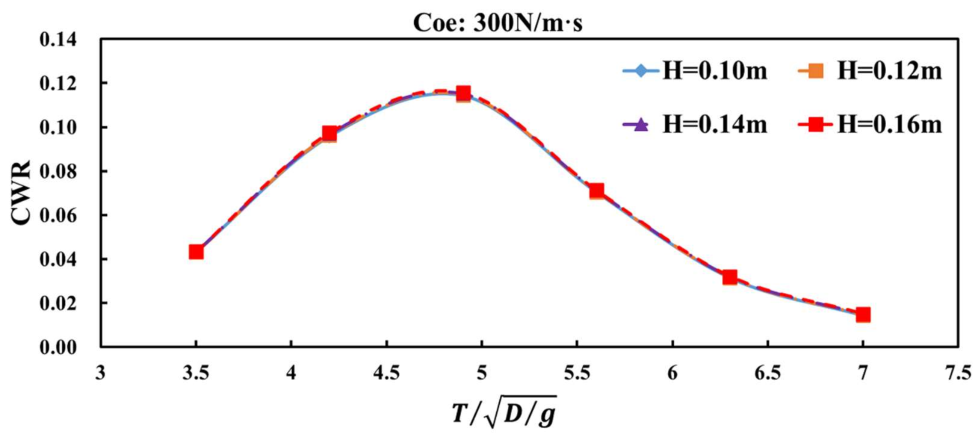

Fig. 14. (d) CWR under linear PTO damping force.

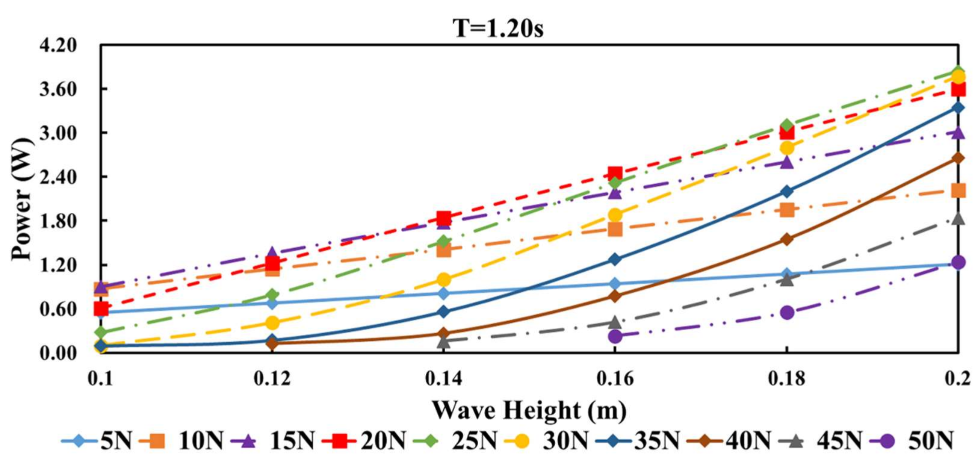

Fig. 15. (a) Capture power under constant PTO damping force.

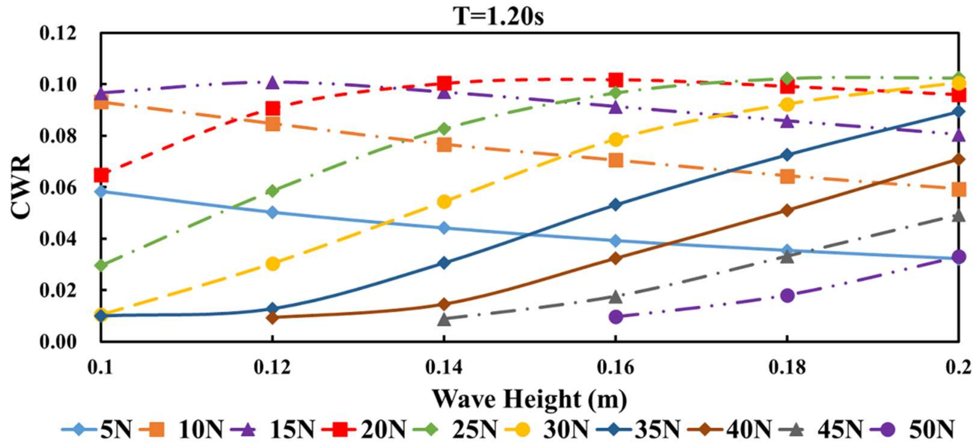

Fig. 15. (b) CWR under constant PTO damping force.

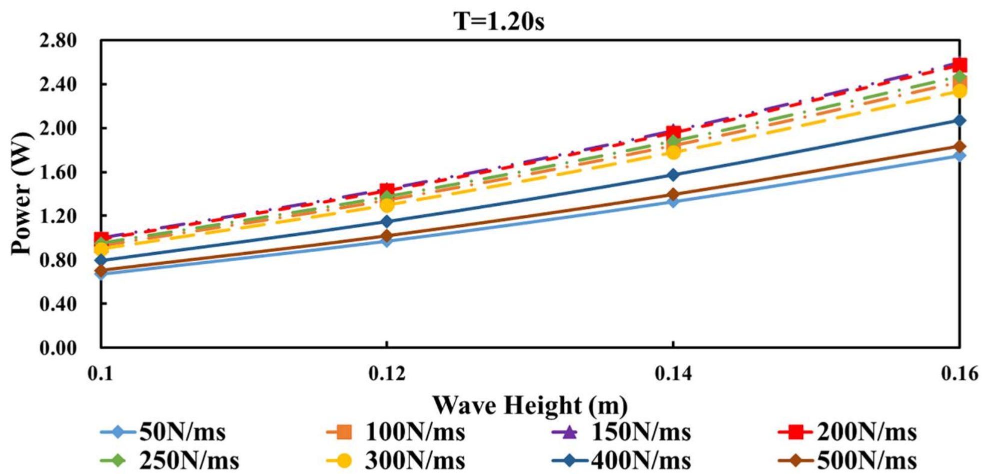

Fig. 15. (c) Capture power under linear PTO damping force.

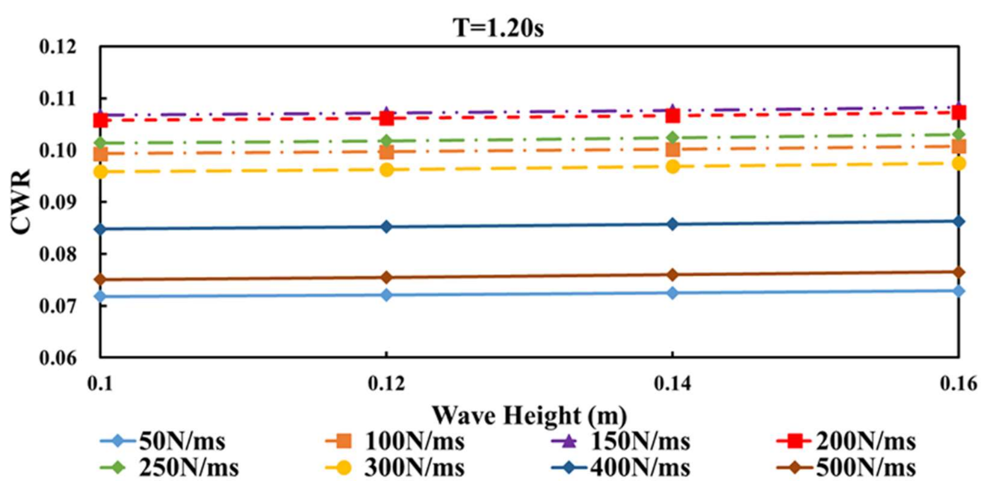

Fig. 15. (d) CWR under linear PTO damping force.

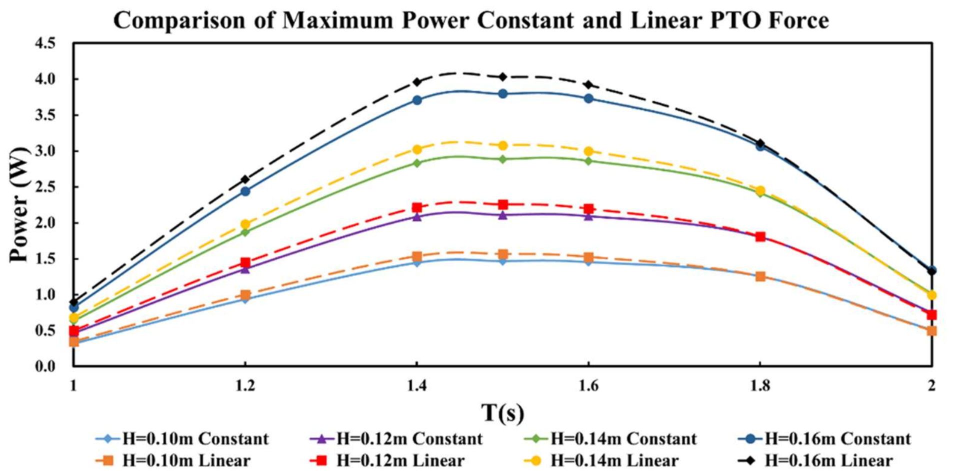

Fig. 16. (a) Comparison of capture power between constant and linear PTO force.

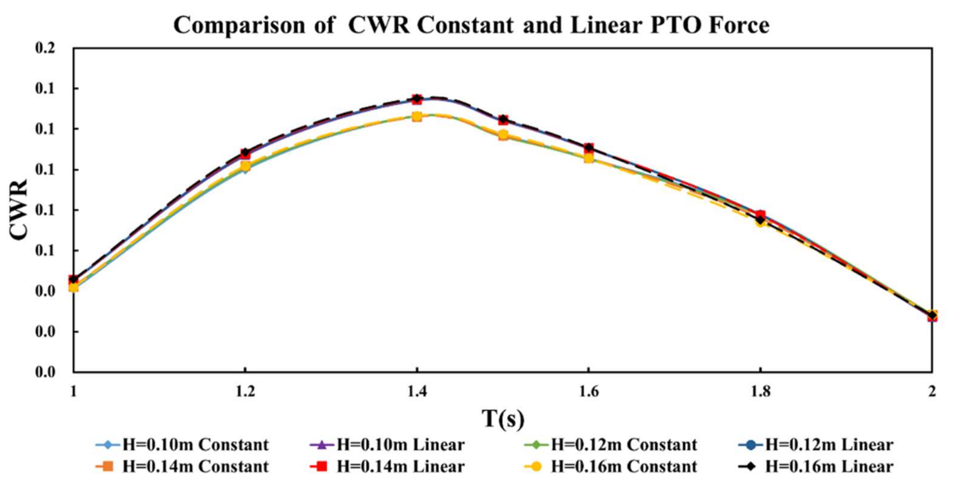

Fig. 16. (b) Comparison of CWR between constant and linear PTO force.

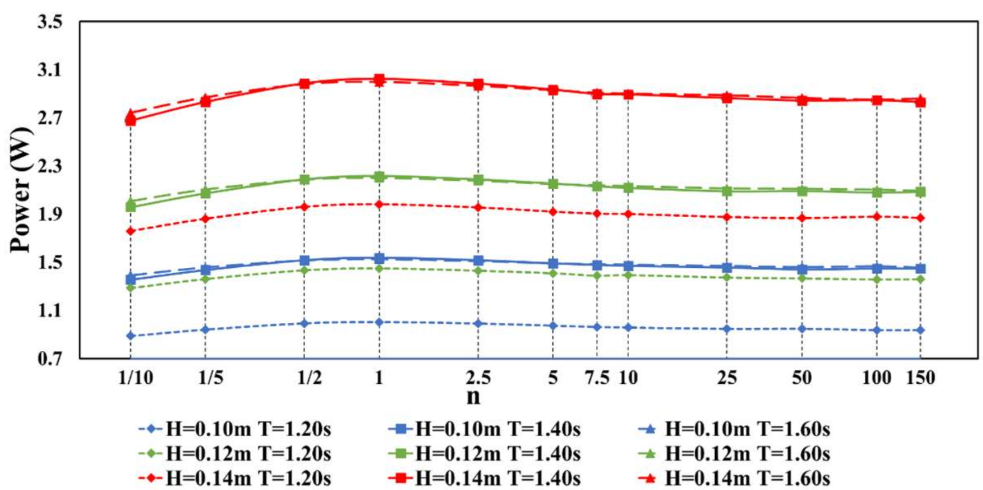

Fig. 17. (a) Capture power as a function of the PTO nonlinear factor.

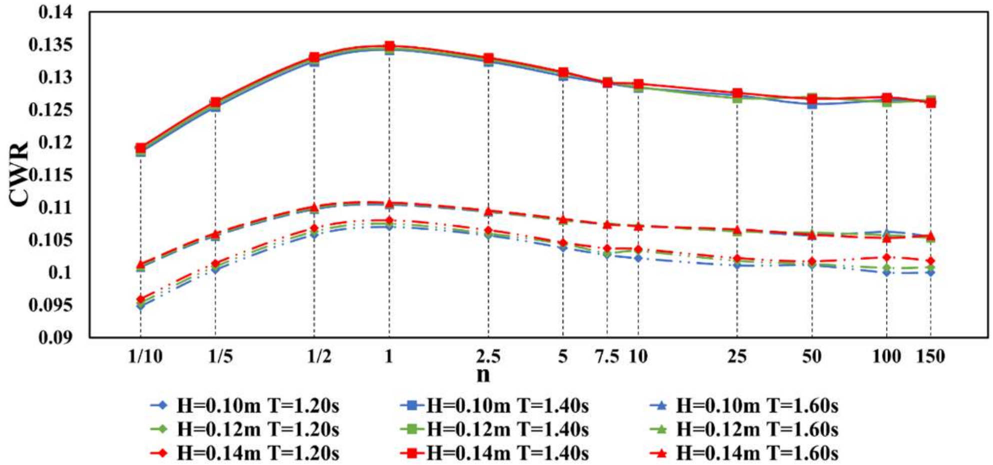

Fig. 17. (b) CWR as a function of the PTO nonlinear factor.

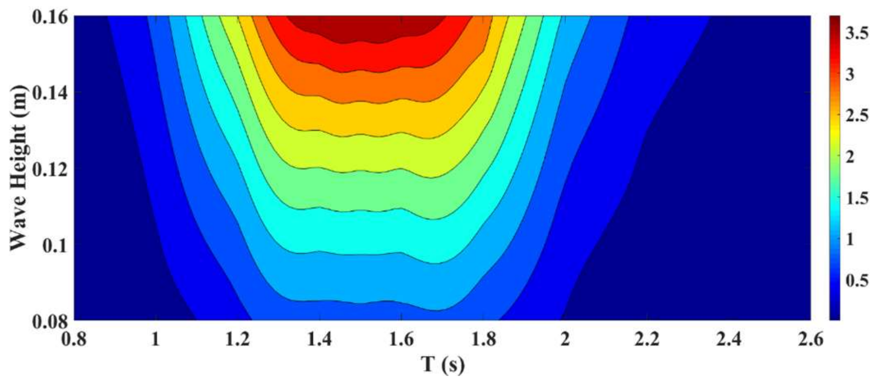

Fig. 18. (a) Capture Power contours with constant PTO force.

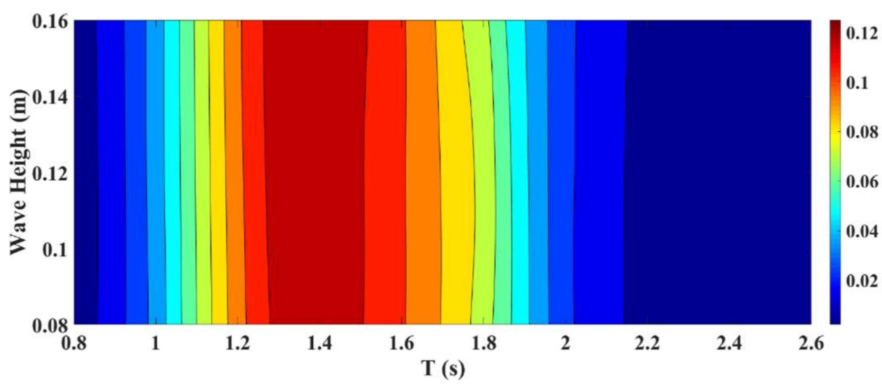

Fig. 18. (b) CWR contours with constant PTO force.

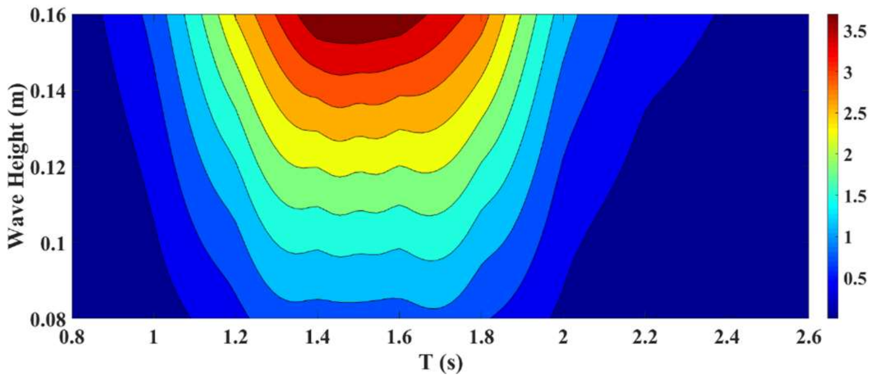

Fig. 18. (c) Capture Power contours with linear PTO force.

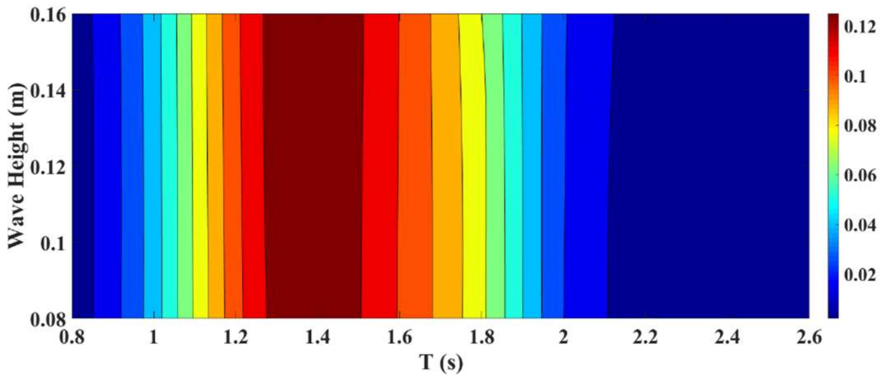

Fig. 18. (d) CWR contours with linear PTO force.

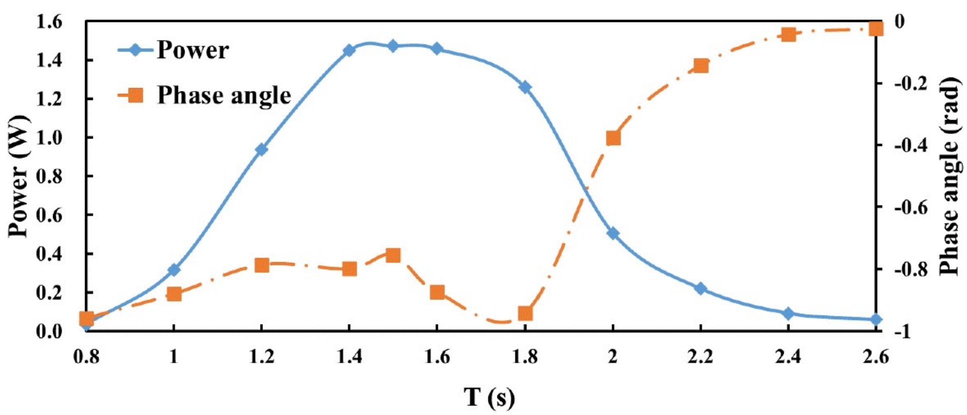

Fig. 19. (a) Power and phase angle with constant PTO force.

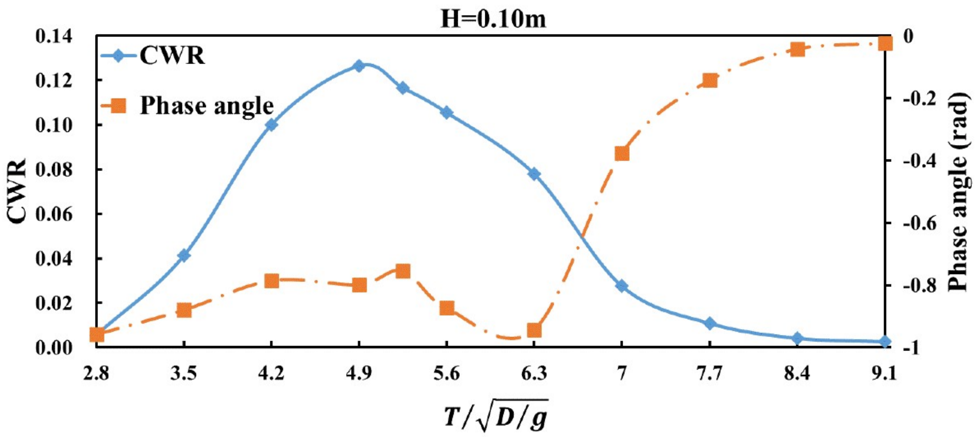

Fig. 19. (b) CWR and phase angle with constant PTO force.

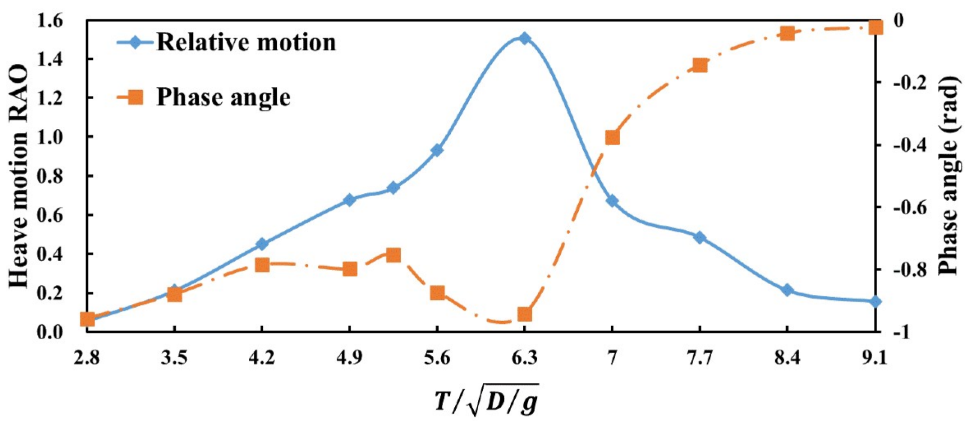

Fig. 19. (c) Relative heave motion RAO and phase angle with constant PTO force.

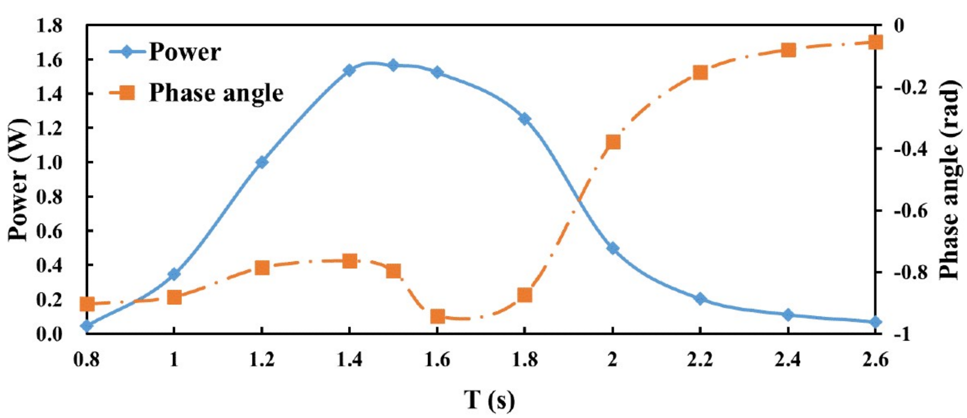

Fig. 19. (d) Power and phase angle with linear PTO force.

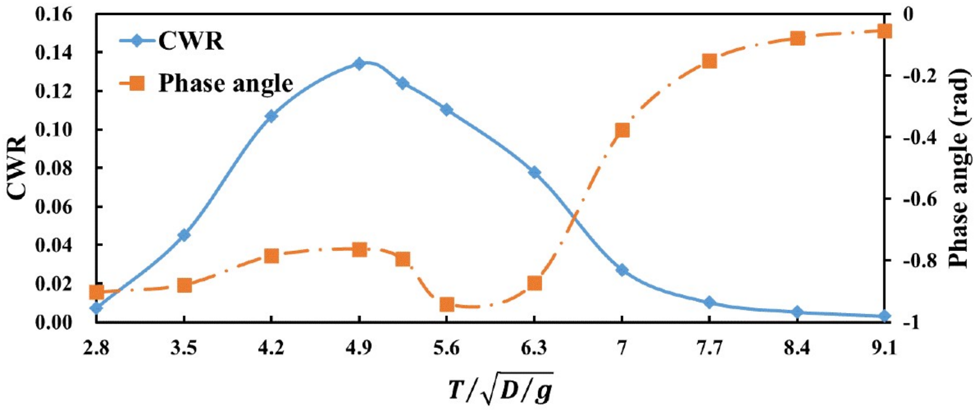

Fig. 19. (e) CWR and phase angle with linear PTO force.

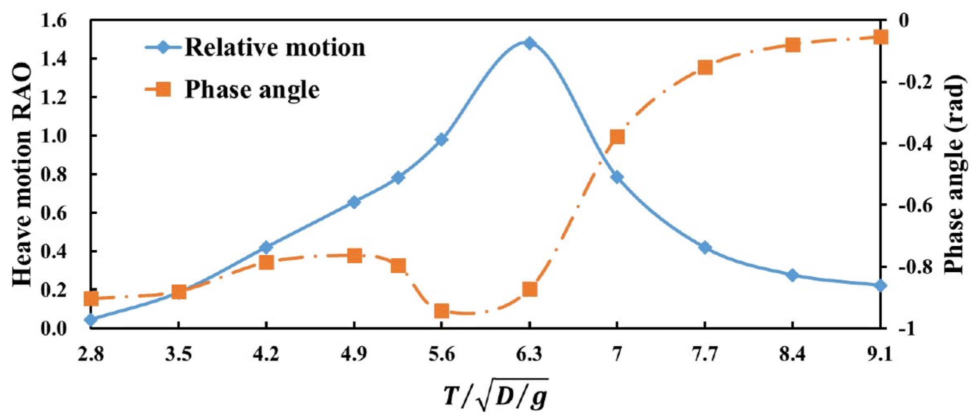

Fig. 19. (f) Relative heave motion RAO and phase angle with linear PTO force.

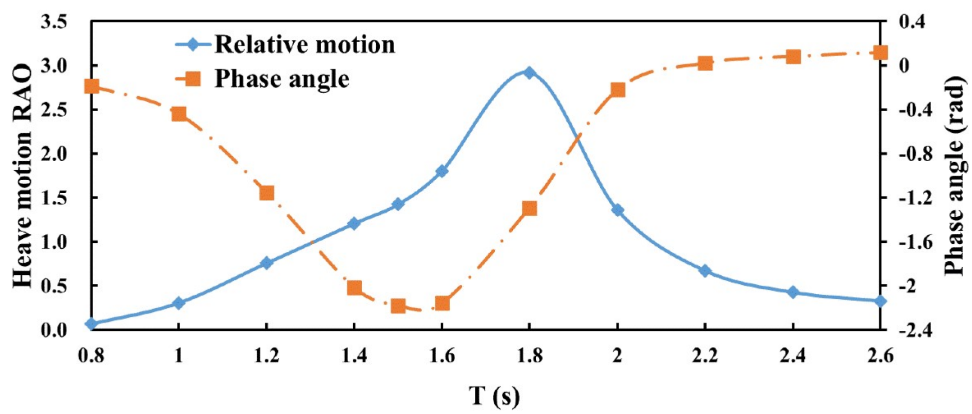

Fig. 19. (g) Relative heave motion RAO and phase angle without PTO force.